

# 1 Subglacial topography and ice flux along the English Coast of 2 Palmer Land, Antarctic Peninsula

3  
4 Kate Winter<sup>1</sup>, Emily A. Hill<sup>1</sup>, G. Hilmar Gudmundsson<sup>1</sup>, John Woodward<sup>1</sup>

5 <sup>1</sup>Department of Geography and Environmental Sciences, Faculty of Engineering and Environment, Northumbria  
6 University, Newcastle upon Tyne, UK

7 *Correspondence to:* Kate Winter (k.winter@northumbria.ac.uk)

8  
9 **Abstract.** Recent satellite data have revealed widespread grounding line retreat, glacier thinning, and associated  
10 mass loss along the Bellingshausen Sea sector, leading to increased concern for the stability of this region of  
11 Antarctica. While satellites have greatly improved our understanding of surface conditions, a lack of radio-echo  
12 sounding (RES) data in this region has restricted our analysis of subglacial topography, ice thickness and ice flux.  
13 In this paper we analyse 3,000 km of 150 MHz airborne RES data collected using the PASIN2 radar system (flown  
14 at 3 – 5 km line spacing) to investigate the subglacial controls on ice flow near to the grounding lines of Ers,  
15 Envisat, Cryosat, Grace, Sentinel, Lidke and Landsat ice streams as well as Hall and Nikitin glaciers. We find that  
16 each outlet is topographically controlled, and when ice thickness is combined with surface velocity data from  
17 MEaSURES (Mouginot et al., 2019), these outlets are found to discharge over  $39.25 \pm 0.79$  Gt a<sup>-1</sup> of ice to floating  
18 ice shelves and the Southern Ocean. Our RES measurements reveal that outlet flows are grounded more than 300  
19 m below sea level, and that there is limited topographic support for inland grounding line re-stabilisation in a  
20 future retreating scenario, with several ice stream beds dipping inland at ~5 degrees per km. These data reinforce  
21 the importance of accurate bed topography to model and understand the controls on inland ice flow and grounding  
22 line position as well as overall mass balance / sea level change estimates. RES data described in this paper are  
23 available through the UK Polar Data Center: [https://doi.org/10.5285/E07D62BF-D58C-4187-A019-](https://doi.org/10.5285/E07D62BF-D58C-4187-A019-59BE998939CC)  
24 [59BE998939CC](https://doi.org/10.5285/E07D62BF-D58C-4187-A019-59BE998939CC) (Corr and Robinson, 2020).

## 25 26 **Short summary**

27 Satellite measurements of the English Coast in the Antarctic Peninsula reveal that glaciers are thinning and losing  
28 mass, but ice thickness data is required to assess these changes, in terms of ice flux, and sea level contribution.  
29 Our ice penetrating radar measurements reveal that low-elevation subglacial channels control fast-flowing ice  
30 streams, which release over 39 gigatons of ice per year to floating ice shelves. This topography could make ice  
31 flows susceptible to future instability.

## 32 **1 Introduction**

33 Remote sensing satellites have increased our awareness and understanding of ice flows in Antarctica since their  
34 inception. In western Palmer Land, on the Antarctic Peninsula, Earth observation satellites have recorded  
35 widespread grounding line retreat (Christie et al., 2016; Konrad et al., 2018) and surface lowering (attributed to  
36 glacier thinning) in the last two decades (Wouters et al., 2015; Hogg et al., 2017; Smith et al., 2020), as well as  
37 surface velocity increases and significant mass loss (e.g. McMillan et al., 2014; Wouters et al., 2015; Martín-  
38 Español et al., 2016; Hogg et al., 2017), where ice flows contribute  $\sim 0.16 \text{ mm a}^{-1}$  to global mean sea level (Wouters  
39 et al., 2015). Regional mass losses of  $-56 \pm 8 \text{ Gt}$  per year between 2010 and 2014 (Wouters et al., 2015) exceed  
40 the magnitude of interannual variability predicted by surface mass balance models (van Wessem et al., 2014,  
41 2016), suggesting that the English Coast of western Palmer Land is undergoing significant change. While satellites  
42 have greatly improved our understanding of surface conditions and changes across Antarctica in recent years, a  
43 lack of ice thickness and subglacial topographic measurements in western Palmer Land has restricted our analysis  
44 of the controls on ice flow, ice flux and grounding line stability along the English Coast (Minchew et al., 2018).  
45 As subglacial topography exerts a strong control over ice flow it is critical to collect and analyse radio-echo  
46 sounding (RES) data close to the grounding line in understudied regions of Antarctica.

47

48 In this paper we present a new, freely available RES dataset along the English Coast of western Palmer Land,  
49 where several outlet glaciers were named after Earth observation satellites in 2019, in deference to the critical role  
50 that satellites have played in measuring and monitoring the Antarctic Ice Sheet (Fig. 1). We combine this new  
51 geophysical dataset with satellite measurements of ice flow speeds from MEaSURES (Mouginot et al., 2019) to  
52 provide an improved picture of the subglacial controls on ice flows draining the English Coast, and directly assess  
53 the improvements to our understanding of bed topography and ice flux in the region as a result of such high-  
54 resolution RES datasets.

55

## 56 **2 Location and previous work**

57 The English Coast of western Palmer Land contains numerous outlet glaciers which flow at speeds of  $\sim 0.5$  to  $2.5$   
58 m per day (Mouginot et al., 2019), from accumulation areas in central Palmer Land, towards ice shelves in the  
59 Bellingshausen Sea sector of Antarctica (Fig.1). A map of surface ice flow speeds in Figure 1 shows how the  
60 recently named Ers, Envisat, Cryosat and Grace ice streams drain into the fast-flowing George VI Ice Shelf, where  
61 floating ice connects Palmer Land to Alexander Island. Further south, Sentinel Ice Stream passes the local  
62 grounding line to form a floating tongue, connected in part to the neighbouring George VI Ice Shelf. Moving  
63 south of George VI Ice Shelf, Hall Glacier, Nikitin Glacier and Lidke Ice Stream each flow into Stange Ice Shelf.  
64 Whilst these outlet flows have separate accumulation zones that border the large Evans Ice Stream catchment  
65 (which drains into the Weddell Sea, on the other side of the Antarctic Peninsula) (Fig.1), their distinct flow units  
66 converge along the English Coast, at the local grounding zone. At the southern extremity of the English Coast,  
67 Landsat Ice Stream flows close to the catchment-defined boundary between the Antarctic Peninsula and West  
68 Antarctica. Slow flowing, almost stagnant ice separates the two tributary flows of Landsat Ice Stream for much  
69 of its length (Mouginot et al., 2019).

70

71 Our understanding of the English Coast of western Palmer Land is driven by data accessibility. Fast ice flow, and  
72 heavily crevassed surfaces have largely restricted in-situ data collection in this region. The first Antarctic-wide  
73 ice thickness and subglacial topography datasets: Bedmap (Lythe et al., 2001) and Bedmap2 (Fretwell et al., 2013)  
74 relied on sparse RES measurements for interpolation in this region of Antarctica. As a result, there are large  
75 uncertainties in bed topography and ice thickness along the English Coast, which limit our understanding of  
76 regional ice dynamics (Minchew et al., 2018). Inaccurate ice thickness and bed topography also hinder our ability  
77 to assess the sensitivity of this region to future change using numerical ice flow models. Previous work has  
78 therefore made use of more readily available satellite data, such as optical images, altimeter data and synthetic  
79 aperture radar (SAR) measurements to assess regional change. Numerous studies have used these detailed datasets  
80 to report on, and model recent changes in surface elevation and ice flow along the Bellingshausen Coast (e.g.  
81 Pritchard et al., 2012; Christie et al., 2016; Hogg et al., 2017; Minchew et al., 2018), as well as Antarctica as a  
82 whole (e.g. Helm et al., 2014; McMillan et al., 2014; Konrad et al., 2018; Smith et al., 2020). Collectively, this  
83 work has highlighted a number of potential vulnerabilities in western Palmer Land. Recent mass loss of George  
84 VI Ice Shelf and Stange Ice Shelf (totalling an estimated  $11 \text{ Gt a}^{-1}$ ) (Rignot et al., 2019) raised concern that English  
85 Coast outlet glaciers could be susceptible to the marine ice sheet instability mechanism (Wouters et al., 2015) -  
86 where grounding-lines have a tendency to accelerate down a retrograde slope in the absence of compensating  
87 forces (like buttressing ice shelves) (Schoof, 2007; Gudmundsson et al., 2012). These concerns are compounded  
88 by recent changes in the grounded ice flows along the English Coast. Wouters et al. (2015) reported an average  
89 surface lowering of  $\sim 0.5 \text{ m a}^{-1}$  along the coastline between 2010-2014, whilst Hogg et al. (2017) calculated a 13%  
90 increase in outlet glacier ice flow between 1993 and 2015. Importantly, if surface thinning and ice flow  
91 acceleration across western Palmer Land continue in the future, dynamical imbalance could lead to further draw  
92 down of the interior ice sheet (like it has done in other areas of Antarctica, (e.g. Shepherd et al., (2002); Rignot  
93 (2008); Konrad et al. (2018)), leading to increased ice discharge into the ocean (Gudmundsson, 2013; Wouters et  
94 al., 2015; Fürst et al., 2016; Kowal et al., 2016; Minchew et al., 2018), with resultant sea level rise. New, high-  
95 resolution measurements of ice thickness and subglacial topography close to the grounding line will improve our  
96 understanding of ice dynamics along the English Coast, and enable more accurate modelling of current conditions,  
97 and forward-looking estimations.

98

### 99 **3 Methods**

100 Data sets outlined in subsections 3.1 – 3.3 are freely available to download. Download links are provided in Sect.7.

101

#### 102 **3.1 Airborne radio echo sounding acquisition, processing, and visualisation**

103 In the austral summer of 2016/2017, the British Antarctic Survey Polarimetric-radar Airborne Science Instrument  
104 (PASIN2) ice sounding radar system was used to acquire  $\sim 3,000$  line km of radio-echo sounding (RES) data along  
105 the English Coast of western Palmer Land, at  $\sim 3 - 5$  km line spacing (Corr and Robinson, 2020). PASIN2 operates  
106 at a frequency of 150 MHz, using a pulse-coded waveform at an effective acquisition rate of 312.5 Hz and a  
107 bandwidth of 13 MHz. Technical details of the RES system are available in Corr et al. (2007). Differential GPS  
108 was used to record aircraft position (with an accuracy better than  $\pm 1$  m) and RES data were collected at an average  
109 flying velocity of  $55 \text{ m s}^{-1}$ . Along-track processing of the data results in an output data rate of 5 Hz, which produces

110 an average spacing between radar traces of 11 m. Section 7 details the information we extract from the online data  
111 repository for use in this paper.

112

113 For the processing of the data, a coherent moving-average filter, commonly referred to as an unfocused SAR, was  
114 used on the range compressed data. The onset of the bed reflector was first automatically picked using first-break  
115 picker of the ProMAX (version 5000.10.0.0; Landmark Software and Services) seismic processing software with  
116 all picks then checked afterwards and corrected by hand if necessary. The delay time of the bed reflector picks  
117 were covered to range using a standard electromagnetic wave propagation speed in ice of  $0.168 \text{ m ns}^{-1}$  and a  
118 correction of 10 m to account for the near-surface high-velocity firn layer (Dowdeswell and Evans 2004; Vaughan  
119 et al., 2006). Ice thickness was calculated by subtracting surface elevation measurements (derived from radar/laser  
120 altimeters for aircraft terrain clearance) from bed reflector depth picks. Internal crossover analysis (measurements  
121 of ice thickness at the same position) yield a standard deviation of 13 m at line intersections, with no systematic  
122 line-to-line biases. Independent crossover analysis, with NASA's airborne Operation IceBridge (OIB) radar data  
123 (Paden et al., 2010) (collected from November 2010 – November 2016), yields a higher standard deviation of 48  
124 m (when high elevation OIB flights are removed from analysis). As this standard deviation is skewed by a  
125 relatively small number of high crossover misfits over steep subglacial topography (where the outlet ice flows are  
126 located), we use the internal crossover analysis value of 13 m for our RES errors.

127

128 RES transects were visualised in 2D in Reflexw radar processing software (version 7.2.2; Sandmeier Scientific  
129 Software) where an energy decay gain was applied to compensate for geometric spreading losses in the radargram  
130 (Daniels et al., 2004). OpendTect seismic interpretation software (version 6.4.0; dGB Earth Sciences) was  
131 employed to plot radargrams in real space using DGPS co-ordinates, to enable three-dimensional analysis of RES  
132 data.

133

### 134 **3.2 Mapping subglacial topography and ice thickness**

135 Airborne RES data presented in this paper have been incorporated in the new BedMachine dataset; a self-  
136 consistent dataset of the Antarctic Ice Sheet based on conservation of mass, which has a resolution of 500 m  
137 (Morlighem, 2019; Morlighem et al., 2019). As a result, data presented in this paper has already been combined  
138 with numerous other RES survey data (including OIB data) to produce continent-wide ice thickness and subglacial  
139 topography maps (Fig. 2b). Whilst Morlighem et al. (2019) report potential vertical errors of  $\sim 100$  m in central  
140 Palmer Land, these values decrease towards the coast, where RES measurements are more frequent (Morlighem,  
141 2019).

142

### 143 **3.3 Surface flow speeds**

144 Surface flow speeds are extracted from MEaSUREs phase-based Antarctica ice velocity map which has a  
145 resolution of 450 m (Mouginot et al., 2019) (Fig. 1a). This data set combines interferometric phases from multiple  
146 satellite interferometric synthetic-aperture radar systems, with additional data, including tracking-derived velocity  
147 to maximise coverage from 1996 to 2018. Across western Palmer Land the average flow speed error is estimated  
148 to be less than  $4 \text{ m a}^{-1}$ .

149

### 150 3.4 Calculating ice flux

151 Using surface flow speeds (Mouginot et al., 2019), and ice thickness measurements from the 1us radargrams in  
152 the online data repository (see Sect. 7), we calculate ice flux across fixed gates delineated for each of the named  
153 ice streams and glaciers along the English Coast (Fig. 2). These flux gates are delineated along RES transects  
154 immediately upstream of the grounding line and they span the width of each outlet. Ice flux ( $q$ ) for each ice stream  
155 or glacier ( $j$ ) is calculated following Eq. (1):

$$156 \quad q_j = \sum_{i=1}^n h_{ij} w_{ij} \vec{v}_{ij} \rho \quad (1)$$

157 where  $i$  is an equally spaced bin along the length of the flux gate,  $w$  is the bin width (which is fixed to 1 m for all  
158 outlets, and is sufficiently small that the solution is not sensitive to a bin width smaller than this),  $\vec{v}$  is the velocity  
159 normal to the flux gate. We use an ice density value of  $\rho = 917 \text{ kg m}^{-3}$ , which is consistent with densities used in  
160 both Bedmap2 and BedMachine datasets (Fretwell et al., 2013; Morlighem, 2019). For simplicity, we are  
161 assuming that surface velocities and ice density are constant with depth. To examine the impact of incorporating  
162 high resolution RES data into gridded bed topography datasets we directly compare ice flux from Bedmap2  
163 (Fretwell et al., 2013) (which has a resolution of 1 km) with the radar picks described in Section 3.1, which are  
164 included in BedMachine (Morlighem, 2019) (Figure 2c). For these calculations we use the same flux gates, phase-  
165 based ice velocities and ice density; simply replacing RES ice thickness for Bedmap2 ice thickness. Using  
166 available errors in velocity and ice thickness datasets we calculate errors in our calculated ice flux ( $\sigma_q$ ) for each  
167 glacier following Eq. (2):

$$168 \quad \sigma_q = \sqrt{\sigma_v^2 + \sigma_h^2} \quad (2)$$

169 where  $\sigma_v = \sum_{i=1}^n h_{ij} w_{ij} d\vec{v}_{ij} \rho$  and  $\sigma_h = \sum_{i=1}^n dh_{ij} w_{ij} \vec{v}_{ij} \rho$  are the contribution of errors in velocity ( $dv$ ) and ice  
170 thickness ( $dh$ ) to the errors in ice flux respectively. Ice flux and associated error bars for each outlet are shown in  
171 Figure 2c.

## 172 4 Results

173 Our airborne RES transects map subglacial topography and ice thickness down the English Coast, from Ers Ice  
174 Stream to Landsat Ice Stream. Whilst our results and discussion focus on 7 major outlets, ice flux from each of  
175 the named outlets is presented in Figure 2. The complete RES dataset (marked in Fig. 1) is freely available to  
176 download from the UK Polar Data Centre (see Sect.7 for more details).

### 177 4.1 Ers Ice Stream

178 Close to the grounding line, Ers Ice Stream reaches a maximum flow speed of just over  $940 \text{ m a}^{-1}$  (averaging out  
179 at  $\sim 2.5 \text{ m per day}$ ) (Mouginot et al., 2019). This ice originates from central Palmer Land (Fig. 1), where ice flows  
180 across the west of the Antarctic Peninsula, towards Ers Ice Stream. In the upper catchment, flow speeds of  $\sim 400$   
181  $\text{m a}^{-1}$  (Mouginot et al., 2019) are recorded along RES transect Ers 6 (Fig 3a). A succession of airborne RES  
182 transects in Figure 3c show how this fast-flowing ice is channelised towards the coast, through a subglacial  
183 depression  $\sim 8 - 14 \text{ km}$  wide. As ice flows through this channel, towards the local grounding line (marked in white

190 on Fig. 3a), ice thickness reduces from a maximum of ~1400 m (along transect Ers 6) to between 580 and 610 m  
191 (along transect Ers 1), where the ice flow is grounded ~400 m below sea level. Ice flux calculated along this radar  
192 transect suggests that Ers Ice Stream contributes over  $7.24 \pm 0.15 \text{ Gt a}^{-1}$  to George VI Ice Shelf (Fig. 2c). Although  
193 this flux gate represents the main trunk of Ers Ice Stream (Fig 2a, 2b), neighbouring ice flow from the lateral  
194 margins of the ice stream (where ice flows at  $\sim 210 - 390 \text{ m a}^{-1}$ ) will, of course, add to this value.

195

#### 196 **4.2 Cryosat Ice Stream**

197 A central flow unit, more than 14 km wide, distinguishes Cryosat Ice Stream from neighbouring regions of slower  
198 flowing ice along the English Coast (Fig. 1). Whilst surrounding ice flows at  $\sim 100 \text{ m a}^{-1}$ , flow speeds in the ice  
199 stream range from 400-500  $\text{m a}^{-1}$  inland (along RES transect Cryosat 3), to  $950 \text{ m a}^{-1}$  ( $\sim 2.6 \text{ m per day}$ ) (Mouginot  
200 et al., 2019) along RES transect Cryosat 1 - which was traversed close to the Antarctic Surface Accumulation and  
201 Ice Discharge (ASAID) grounding line (Bindschadler et al., 2011) (Fig. 4a). Figure 4a shows how the main flow  
202 of Cryosat Ice Stream is joined by a smaller tributary to the south, where ice flow speeds increase from  $180 \text{ m a}^{-1}$   
203 along transect Cryosat 4 to over  $400 \text{ m a}^{-1}$  (Mouginot et al., 2019) along transect Cryosat 1 (traversed  $\sim 5 \text{ km}$   
204 from the ASAID grounding line). In both flow units, the subglacial bed remains well below sea level along the  
205 length of each transect. Close the grounding line, along transect Cryosat 1, the glacial bed is between 450 and 800  
206 m below sea level, where overlying ice is 500 – 900 m thick. Although subglacial topographic depressions are  
207 visible in-land (where subglacial peaks which reach over 500 m from the bed help to define the low elevation  
208 topography), subglacial troughs become more defined towards the coast, where ice is guided through several  
209 almost U-shaped troughs (Fig. 4b). This is most obvious in RES transect Cryosat 1, where the main flow of ice is  
210 channelled through a  $\sim 14 \text{ km}$  wide, 300 m deep subglacial trough close to the local grounding line, whilst the  
211 smaller (southern) tributary flow is directed through a  $\sim 400 \text{ m}$  deep trough, which is  $\sim 3 \text{ km}$  wide at its base (Fig.  
212 4b). The flow units of Cryosat Ice Stream collectively discharge  $5.99 \pm 0.14 \text{ Gt a}^{-1}$  of ice across the grounding  
213 line. The ice flux profile in Fig. 4b shows how much of this flux is discharged through the deep and fast flowing  
214 central sector of the ice stream, rather than the deeper southern tributary.

215

#### 216 **4.3 Sentinel Ice Stream**

217 In the MEaSURES velocity map, Sentinel Ice Stream appears to have the widest outflow of the English Coast,  
218 reaching a width of over 20 km. The main trunk of the ice stream curves round from an almost southerly flow  
219 direction, to a more westerly direction along its length (Fig. 4c) as ice flow speeds increase from  $\sim 350 \text{ m a}^{-1}$  (along  
220 RES transect Sentinel 5) to  $\sim 800 \text{ m a}^{-1}$  (closer to the grounding zone, along transect Sentinel 1) (Mouginot et al.,  
221 2019). Whilst the subglacial bed remains well below sea level in all transects (at elevations in the region of -500  
222 to -680 m), fluctuations in subglacial topography and ice thickness are recorded along and down flow in successive  
223 RES transects (Fig. 4d). The largely unconfined ice flow in transect Sentinel 5 becomes more confined down flow  
224 due to the emergence of higher elevation subglacial topography along the lateral margins of Sentinel Ice Stream.  
225 These subsurface conditions are concurrent with ice thickness measurements (where maximum ice thickness  
226 decreases down flow, from  $\sim 1200 \text{ m}$  in transect Sentinel 5 to  $\sim 550 \text{ m}$  in Sentinel 1), as well as surface velocity  
227 measurements, which reveal increasing flow speeds in the central trunk of Sentinel Ice Stream with distance down  
228 flow. The total flux of Sentinel Ice Stream is  $6.01 \pm 0.14 \text{ Gt a}^{-1}$ . Whilst this flux will be added to by flow from the  
229 south (where enhanced flow speeds are recorded, but they are about three times slower than the central trunk of

230 Sentinel Ice Stream), there will be much less flux in the north, where ice flows at a few tens of metres per year  
231 (Mouginot et al., 2019) (Fig. 4c), over higher elevation subglacial topography (~400 m higher than the base of the  
232 subglacial trough).

233

#### 234 **4.4 Hall Glacier**

235 Hall Glacier is the most northern tributary flow of the Stange Ice Shelf (Fig. 1). Surface flow speeds increase from  
236 RES transect HNL 6 (close to the onset of streaming flow) - where ice flows just over  $100 \text{ m a}^{-1}$ , to RES transect  
237 HNL 1 (~1.5 – 9.5 km from the ASAID grounding line and 14 km from HNL 6), where ice flow speeds reach  $380$   
238  $\text{m a}^{-1}$  (Mouginot et al., 2019) (Fig. 5a). These enhanced flow speeds clearly differentiate Hall Glacier from the  
239 almost stagnant neighbouring ice flow ( $<10 \text{ m a}^{-1}$ ) along its lateral margins in Figure 5a. This figure shows how  
240 the fast-flowing portion of the outlet glacier decreases in width from ~15 km inland to ~8 km along RES transect  
241 HNL 2. This reduction in width coincides with a change in subsurface topography and ice thickness (Fig. 5c).  
242 Whilst a shallow subglacial depression is apparent upstream, in RES transect HNL 5 (where the subglacial bed is  
243 ~500 m below sea level and ice thickness reaches a maximum of 750 m), a much deeper channel is recorded down  
244 flow, where ice up to 930 m thick is channelised through high elevation subglacial topography. The profile in  
245 Figure 5b (derived from the flux gate marked on Figure 5a) shows the impact this subglacial topography and ice  
246 thickness has on ice flux. Flux is greatest along the central trunk of Hall Glacier where a ~7 km wide subglacial  
247 channel supports ice flow speeds of more than  $350 \text{ m a}^{-1}$  (Mouginot et al., 2019). Over the whole flux gate, Hall  
248 Glacier contributes  $\sim 1.87 \pm 0.04 \text{ Gt a}^{-1}$  of ice to the Stange Ice Shelf, which drains into the Bellingshausen Sea  
249 sector of the Southern Ocean.

250

#### 251 **4.5 Nikitin Glacier**

252 Situated between Hall Glacier and Lidke Ice Stream, Nikitin Glacier maintains flow speeds in the region of 200-  
253  $450 \text{ m a}^{-1}$  (Mouginot et al., 2019), as ice flow from central Palmer Land begins to stream towards the Stange Ice  
254 Shelf (Fig. 5). For much of its length, Nikitin Glacier flows through a 15 km wide subglacial channel, where ice  
255 thicknesses up to 1000 m flow over a glacial bed situated well below sea level (with elevations of -400 to -700  
256 m). This low-elevation subglacial topography combined with thick ice flows and enhanced ice flow speeds enable  
257 Nikitin Ice Stream to contribute over  $2.13 \pm 0.05 \text{ Gt a}^{-1}$  of ice to the Stange Ice Shelf. Whilst it is difficult to  
258 precisely define the point at which this ice begins to float in our radargrams, it is worth noting that complex and  
259 highly reflective RES returns beneath Nikitin Ice Stream in transect HNL 1 suggest that the ice stream could be  
260 afloat here. This finding is coincident with the positioning of the ASAID grounding line (Bindschadler et al.,  
261 2011) (marked as a white line in Figure 5a), which is derived from satellite data.

262

#### 263 **4.6 Lidke Ice Stream**

264 The MEaSURES dataset (Mouginot et al., 2019) presented in Figure 5a, shows how Lidke Ice Stream is fed by  
265 two tributary flows which coalesce close to RES transect HNL 4, where ice begins to flow along a central trunk  
266 at flow speeds in the region of  $350 - 420 \text{ m a}^{-1}$  (Fig. 5a). Although Lidke Ice Stream is linked to neighbouring  
267 Nikitin Ice Stream in its upper catchment, a clear separation between the two ice streams is recorded down flow,  
268 where the enhanced flow units become separated by a region of almost stagnant ice ( $< 10 \text{ m a}^{-1}$ ). RES transects  
269 in Figure 5c show how this slow-moving ice sits on top of relatively high elevation subglacial topography (with

270 elevations of -380 to -500 m). This raised topography helps to define the northern margin of Lidke Ice Stream,  
271 which flows through much lower elevation subglacial topography, situated ~600 – 800 m below sea level.

272

273 In RES transects HNL 4 and HNL 5 (traversed close to the onset of streaming flow) numerous peaks and troughs  
274 dominate the subglacial topography returns, resulting in spatially variable ice thickness and ice flux. However,  
275 further down flow, and closer to the grounding line, subglacial topography is more subdued, with the emergence  
276 of a depressed subglacial channel (reaching a maximum depth of 810 m below sea level), where ice up to 1250 m  
277 thick achieves surface flow speeds in the region of  $400 \text{ m a}^{-1}$  (Mouginot et al., 2019) at the grounding zone. In a  
278 flux gate along HNL3 (marked in Fig. 5a), Lidke Ice Stream is calculated to contribute  $>2.71 \pm 0.01 \text{ Gt a}^{-1}$  to the  
279 Stange Ice Shelf. The flux profile in Figure 5b shows how this value is distributed across the glacier – with high  
280 flux values recorded in areas which have low elevation subglacial topography, thicker ice, and fast ice flow.

281

#### 282 **4.7 Landsat Ice Stream**

283 Landsat Ice Stream (situated close to the catchment-defined boundary between the Antarctic Peninsula and West  
284 Antarctica) is formed of a northern and southern tributary, with ice flow converging at, or close to the ASAD  
285 grounding line (Fig. 6). Both tributaries have similar characteristics: they each reach flow speeds in excess of  $500$   
286  $\text{m a}^{-1}$  in the centre of the ice flow (along RES transect Landsat 3) before flow begins to accelerate downstream (to  
287 over  $700 \text{ m a}^{-1}$  near transect Landsat 1) (Mouginot et al., 2019). Between the two tributaries, flow speeds are much  
288 lower, ranging from  $40 \text{ m a}^{-1}$  (25 km inland of the grounding line), to  $\sim 100 \text{ m a}^{-1}$  (along RES transect Landsat 1,  
289 traversed close to the local grounding line) (Mouginot et al., 2019). A sequence of airborne RES transects in  
290 Figure 6c show that these flow speeds reflect subglacial topography. Both tributaries flow through deep subglacial  
291 basins (situated  $\sim 700 \text{ m}$  below sea level), where ice flows up to 900 m thick are increasingly channelised towards  
292 the coast by higher subglacial topography along the ice stream's lateral margins. Along RES transect Landsat 2,  
293 ice flux gates across the north and south tributary flows combine to produce a total ice flux of  $7.23 \pm 0.13 \text{ Gt a}^{-1}$ .  
294 Between these two flow units ice flux is substantially lower, because of lower surface flow speeds, elevated  
295 subglacial topography, and reduced ice thickness.

296

### 297 **5 Discussion**

298 English Coast ice streams and glaciers contribute over  $39.25 \pm 0.79 \text{ Gt a}^{-1}$  of ice to floating ice shelves in the  
299 Bellingshausen Sea. This ice flows from the center of Palmer Land, towards the coast, where discrete ice flows  
300 develop in line with, and as a result of depressed subglacial topography - in a region of Antarctica where the  
301 glacial bed is situated well below sea level. In the following paragraphs, we briefly discuss the main features of  
302 each major ice stream (documented in the results) from north to south. The significance of the radar data set is  
303 presented in Sect. 6.

304

#### 305 **5.1 Ers Ice Stream**

306 Ers Ice Stream, at the northern extremity of our study site, produces the largest ice flux of all English Coast ice  
307 streams (Fig. 2c). This is the result of elevated surface flow speeds (Mouginot et al., 2019), substantial ice  
308 thicknesses and pronounced subglacial topography, which, for the most part, channelises ice through a wide  
309 subglacial depression (Fig. 3c). Enhanced ice flow is also recorded on either side of the subglacial channel, where



310 surface flow speeds greater than  $100 \text{ m a}^{-1}$  (Mouginot et al., 2019) contribute over  $1 \times 10^4 \text{ Gt}$  of ice to George  
311 VI Ice Shelf per year. This enhanced ice flow makes it difficult to precisely map the lateral margins of the ice  
312 stream and fully assess the individual contribution of Ers Ice Stream to English Coast ice flux. However, it is clear  
313 that this area of the English Coast contributes substantial and continued ice flux to George VI Ice Shelf, as a result  
314 of high surface flow speeds, thick ice and deep subglacial topography.

315

## 316 **5.2 Cryosat Ice Stream**

317 Although ice flux from Cryosat Ice Stream is more than 50% lower than neighbouring Ers Ice Stream, it boasts  
318 the greatest surface flow speeds of the English Coast: flowing at a maximum of  $950 \text{ m a}^{-1}$  (Mouginot et al., 2019)  
319 (averaging out at  $\sim 2.6 \text{ m per day}$ ). These enhanced ice flow speeds are recorded along the width of the ice stream,  
320 where thick ice flows through, and over multiple, deep incisions in the basal topography (Fig. 4b). Fig. 4a shows  
321 how these ice flow speeds are maintained across the grounding zone, as ice flows into George VI Ice Shelf. As  
322 the ice shelf buttresses the inland ice flow of Cryosat Ice Stream, further thinning of the ice shelf could reduce  
323 resistive stress (buttressing) at the grounding line, subsequently increasing ice discharge in this region (Tsai et al.,  
324 2015; Minchew et al., 2018).

325

## 326 **5.3 Sentinel Ice Stream**

327 Pronounced topographic depressions in most of the cross-flow radar lines that transect Sentinel Ice Stream (Fig.  
328 4d) suggest a degree of topographic confinement for Sentinel Ice Stream, which is grounded more than 500 m  
329 below sea level. Whilst this confinement helps to channelise  $6.00 \text{ Gt a}^{-1}$  of ice towards the local grounding line  
330 currently, along-flow radargrams in Figure 7a show how the ice stream might respond to future ingress of the  
331 grounding line position (e.g. Christie et al., 2016). Ice stream thickness fluctuates in conjunction with subglacial  
332 topography down the main trunk of the ice stream - from the upper catchment of the ice stream to the floating ice  
333 tongue, which is recorded by bright, white RES reflectors in Fig, 7a. These bright reflectors help to highlight the  
334 grounding zone (MacGregor et al., 2011), where ice flexes in response to tidal modulation (e.g. Rosier and  
335 Gudmundsson, 2018). Annotations in Figure 7a point out a range of previously unknown subglacial features  
336 beneath Sentinel Ice Stream, like reverse subglacial slopes close to the grounding zone (which decline inland at  
337  $\sim 5.5 - 4.5^\circ \text{ per km}$ ), as well as more raised topographic features further inland. These measurements are critical  
338 for simulations of grounding line retreat. They show that a retreat of the grounding line into deeper water could  
339 allow thicker ice to reach floatation, which would increase glacier driving stress and ice flux across the grounding  
340 line (Tsai et al., 2015), with immediate implications for ice flow speed, ice discharge, and meltwater contribution  
341 to the Southern Ocean (Minchew et al., 2018). RES measurements inland of the present-day grounding line reveal  
342 a steep reverse bed-slope, which after an initial retreat of the grounding line (due to some forcing) could promote  
343 unstable (runaway) grounding retreat (e.g. Schoof 2007; Jamieson et al., 2012; Kleman and Applegate, 2014).  
344 However, elevated subglacial topography  $\sim 10 \text{ km}$  inland of the current grounding line could potentially act as a  
345 pinning point for future ice stream re-grounding (Favier et al., 2016) (Fig, 7a). Our RES measurements will allow  
346 these potential instabilities to be explored in new, high-resolution numerical modelling simulations.

347

## 348 **5.4 Hall Glacier, Nikitin Glacier and Lidke Ice Stream**

349 Further down the English Coast, Hall Glacier, Nikitin Glacier and Lidke Ice Stream are clearly discernible in  
350 maps of surface ice flow speeds (Mouginot et al., 2019) (Fig. 1) and subsurface topography maps, like Bedmap2  
351 (Fretwell et al., 2013) and the newer, higher resolution BedMachine (Morlighem et al., 2019) (Fig. 2). These maps  
352 show how discrete ice flow units develop in accordance with subglacial depressions, where elevated subglacial  
353 topography between tributaries help to promote independent, channelised ice flow towards the coast (Fig. 5). All  
354 three ice flows converge in the floating Stange Ice Shelf, where they release a combined ice flux of  $\sim 6.72 \text{ Gt a}^{-1}$ .  
355 The zone between grounded and floating ice is discernible in satellite data (Bindschadler et al., 2011) (noted by  
356 the ASAID grounding line in Figure 5a) and in our RES dataset, where bright subglacial reflections suggest water  
357 ingress (MacGregor et al., 2011) along line HNL 1 (Fig. 5). These independent data sets mark the same grounding  
358 zone position along the English Coast. Whilst our radargrams do not extend seaward of transect HNL 1, we  
359 hypothesise that the 8 km digression of the ASAID grounding line in Figure 5a could reflect the subglacial  
360 extension of the deep subglacial trough beneath Hall Glacier. This relative extension of the grounding line shows  
361 the impact subglacial troughs can have on grounding line location and potentially grounding line stability (as  
362 noted in other regions of Antarctica, by Jamieson et al. (2012)). Should the grounding line migrate in the future,  
363 relatively small-scale subsurface features like these could result in substantially different reactions from  
364 neighbouring ice flows, like Hall Glacier, Nikitin Glacier and Lidke Ice Stream.

365

### 366 **5.5 Landsat Ice Stream**

367 The final radar transects in our survey were flown across Landsat Ice Stream (Fig. 6). These radargrams reveal  
368 topographically confined ice flow along two discrete tributaries (north and south) for more than 15 km. These ice  
369 streams, which flow at speeds greater than  $500 \text{ m a}^{-1}$  (Mouginot et al., 2019) contribute over  $7.23 \text{ Gt a}^{-1}$  of ice to  
370 the Bellingshausen Sea. Along-flow lines presented in Figure 7b show the differences in ice thickness and  
371 subglacial topography between the north and south tributaries of Landsat Ice Stream, which are each grounded  
372 more than 700 m below sea level. The north tributary flows across a remarkably flat bed for most of its length,  
373 but this is punctuated by a region of elevated subglacial topography  $\sim 5 \text{ km}$  inland of the current grounding line,  
374 which is  $\sim 100 \text{ m}$  higher than surrounding bed returns (Landsat 6 transect, Fig. 7b). Whilst this generally flat, low-  
375 elevation subglacial bed could enable rapid grounding line retreat in response to mass balance changes and/or  
376 applied oceanic forcings (Weertman, 1974; Jamieson et al., 2012), this region of elevated subglacial topography  
377 could act as a temporary pinning point for re-grounding in a retreating ice sheet scenario. A similar potential  
378 pinning point is located much further inland of the grounding zone on the south tributary of Landsat Glacier (RES  
379 transect Landsat 7, Fig. 7b). Here, flat subglacial topography (situated  $\sim 600 \text{ m}$  below sea level) extends  $\sim 12 \text{ km}$   
380 inland of the current grounding line, until bed topography lowers slightly and then inclines by  $120 \text{ m}$  over  $2 \text{ km}$ .  
381 Beyond this point, there is a reverse slope, dipping inland at  $3.5^\circ$  per km. This subglacial topography correlates  
382 with satellite-derived surface ice flow speeds (recorded by Mouginot et al., 2019): enhanced flow is recorded  
383 along RES transect Landsat 1, where bright subglacial reflectors suggest the presence of subglacial water  
384 (MacGregor et al., 2011). These reflections, which extend inland of the ASAID grounding line could provide the  
385 subglacial evidence to corroborate recent satellite-derived measurements of inland grounding-line migration in  
386 this region of Antarctica (Christie et al., 2016; Konrad et al., 2018). As warm circumpolar deep water resides at  
387  $\sim 300 \text{ m}$  depth in the neighbouring ocean (Kimura et al, 2015) any relatively warm water ingress inland could

388 promote ice dynamical imbalance in this region of Antarctica and lead to further drawdown of ice from the interior  
389 (as reported by Hogg et al., 2017).

390

## 391 **6 Significance of the dataset**

392 Our RES data set provides the scientific community with over 3,000 km of airborne RES data along the English  
393 Coast of the Antarctic Peninsula. The density of transects (at 3 – 5 km line spacing), and coverage so close to the  
394 grounding line is unusual. Resultant latitude, longitude and elevation data (available from the Polar Data Centre)  
395 adds considerable ice thickness and subglacial topographic information to this area of Antarctica, where pre-  
396 existing and reliable ice penetrating radar data sets are more infrequent than other regions of the continent (like  
397 central Graham Land or Pine Island Glacier). Ice flux calculated along English Coast outlet streams using our new  
398 RES measurements yields a total ice flux of  $39.25 \pm 0.79 \text{ Gt a}^{-1}$ , across a combined flux gate length of 178 km.  
399 This is approximately half of the basin wide flux calculation ( $78 \text{ Gt a}^{-1}$ ) presented by Gardner et al. (2018) who  
400 used a much longer flux gate along the English Coast of  $\sim 550 \text{ km}$ . This quick comparison between ice flux datasets  
401 (which utilise different bed topography and ice velocity inputs) suggests that the outlets recorded in this study  
402 provide the major contributions to basin-wide flux. Figure 2c compares the ice flux calculated using our new RES  
403 measurements to flux estimates that we derive from the pre-existing Bedmap2 and BedMachine ice thickness  
404 datasets. In general, our total ice flux is in good agreement with both datasets which record  $39.82 \pm 7.1 \text{ Gt a}^{-1}$   
405 (Bedmap2) and  $38.49 \pm 2.95 \text{ Gt a}^{-1}$  (BedMachine). Despite this agreement, we note higher overall errors in these  
406 compilations (which have imperfect fidelity to radar observations, and different uncertainty estimates), as well as  
407 regional discrepancies, particularly when using Bedmap2 ice thickness measurements. Along the upper stretch of  
408 the English Coast (Ers, Envisat, Cryosat, Grace and Sentinel ice streams, and Hall Glacier), Bedmap2  
409 overestimates ice flux by  $\sim 1.71 \text{ Gt a}^{-1}$  and along the southern outflows (Nikitin Glacier, Lidke Ice Stream and  
410 Landsat Ice Stream) Bedmap2 underestimates ice flux by  $\sim 1.14 \text{ Gt a}^{-1}$ , compared to our RES ice thickness  
411 measurements. Due to the coarse resolution and limited number of RES measurements incorporated in Bedmap2,  
412 errors in ice thickness are on the order of hundreds of metres and range from 13-45% of total ice thickness across  
413 our flux gates. In comparison, the errors associated with ice thickness measurements in BedMachine are  
414 significantly smaller (2-13%), and ice flux at individual outlets are in better agreement with the RES flux estimates  
415 (Figure 2c). This demonstrates that including new high-resolution RES measurements in BedMachine  
416 (Morlighem, 2019) has greatly improved the resolution and accuracy of the latest continent-wide subglacial  
417 topography and ice thickness map (Figure 2).

418

419 Accurate, high resolution ice thickness and subglacial bed measurements like the ones we present in this paper  
420 are crucial for understanding ice flow and modelling ice dynamics. It must therefore remain a future research  
421 priority to collect more RES data across the Antarctic Ice Sheet, and target regions that remain geophysically  
422 understudied. This data will significantly improve continent-wide compilations of ice thickness and subglacial  
423 topography. These RES measurements should be collected along- and across-flow to capture small-scale  
424 topographic perturbations in the subglacial bed (e.g. Figure 7), which are critical for assessing the potential for  
425 grounding line retreat and marine ice sheet instability.

426

## 427 **7 Data Availability**

428 Radio echo sounding data used in this paper, from Corr and Robinson (2020) are available through the UK Polar  
429 Data Center: <https://doi.org/10.5285/E07D62BF-D58C-4187-A019-59BE998939CC>. In this paper we present  
430 and discuss the 1 micro-second SEGY data. Data related to Ers Ice Stream, Envisat Ice Stream and Cryosat Ice  
431 Stream can be found in file F25a. File F26b provides information for Grace Ice Stream and Sentinel Ice Stream.  
432 File F28a provides data across Hall Glacier, Nikitin Glacier and Lidke Ice Stream and File F29a provides data for  
433 Landsat Ice Stream. Note that the location of radargrams (close to the grounding line) and enhanced flow speeds  
434 in the area limit radio-stratigraphy analysis for direct tracing and continuity applications. Data related to surface  
435 ice velocity from MEaSURES (Mouginot et al., 2019) can be downloaded here: [https://nsidc.org/data/NSIDC-  
436 0754/versions/1](https://nsidc.org/data/NSIDC-0754/versions/1). Maps of subglacial topography and ice thickness can be accessed from the BedMachine  
437 repository (Morlighem, 2019): <https://nsidc.org/data/nsidc-0756>.

438

## 439 **8 Conclusions**

440 Ice penetrating radar transects along the English Coast of western Palmer Land in the Bellingshausen Sea sector  
441 of the Antarctic Peninsula reveal multiple topographically confined ice flows, grounded ~300 – 800 m below sea  
442 level. New ice thickness data, combined with satellite derived surface flow speeds from MEaSURES (Mouginot  
443 et al., 2019) allow us to improve ice flux calculations along the recently named Ers, Envisat, Cryosat, Grace,  
444 Sentinel and Landsat ice streams as well as the previously titled Hall and Nikitin glaciers and Lidke Ice Stream.  
445 At a time when satellites are recording widespread grounding line retreat (Christie et al. 2016; Konrad et al.,  
446 2018), surface lowering (attributed to glacier thinning) (Wouters et al., 2015; Hogg et al., 2017; Smith et al., 2020)  
447 and significant mass loss (McMillan et al., 2014; Wouters et al., 2015; Martín-Español et al., 2016; Hogg et al.,  
448 2017) along the English Coast, our radio-echo-sounding (RES) dataset provides the high resolution ice thickness,  
449 and subglacial topography data required for change detection. These measurements and analysis will improve  
450 simulations of Antarctic coastal change and associated global sea level estimations.

451

## 452 **Author contributions**

453 All authors contributed to the writing and editing of the paper. K. Winter was the principal investigator of the  
454 project, which was instigated by G. H. Gudmundsson and guided by J. Woodward. Ice flux calculations were  
455 provided by E. A. Hill.

456

## 457 **Competing Interests**

458 The authors declare that they have no conflict of interest.

459

## 460 **Acknowledgements**

461 RES data were collected by the British Antarctic Survey aerogeophysical group in the austral summer of  
462 2016/2017 and data were pre-processed by Hugh F. J. Corr (British Antarctic Survey). We acknowledge the  
463 support of Landmark Software and Services, a Landmark Company for the use of ProMAX software. We thank  
464 all those involved in the process of planning and collecting data, as well as helpful manuscript reviews from  
465 Joseph MacGregor and an anonymous reviewer.

466

467

468 **References**

- 469 Bindschadler, R., Choi, H., Wichlacz, A., Bingham, R., Bohlander, J., Brunt, K., Corr, H. F. J.,  
470 Drews, R., Fricker, H., Hall, M., Hindmarsh, R., Kohler, J., Padman, L., Rack, W., Rotschky, G.,  
471 Urbini, S., Vornberger, P., and Young, N.: Getting around Antarctica: new high-resolution  
472 mappings of the grounded and freely-floating boundaries of the Antarctic ice sheet created for the  
473 International Polar Year, *The Cryosphere*, 5, 569-588, <https://doi.org/10.5194/tc-5-569-2011>,  
474 2011.
- 475 Christie, F. D. W., Bingham, R., Gourmelen, N., Tett, S. F. B., and Muto, A.: Four-decade  
476 record of pervasive grounding line retreat along the Bellingshausen margin of West Antarctica,  
477 *Geophysical Research letters*, 43, 5741-5749, <https://doi.org/10.1002/2016GL068972>, 2016.
- 478 Corr, H., Ferraccioli, F., Frearson, N., Jordan, T. A., Robinson, C., Armadillo, E., Caneva, G., Bozzo, E., and  
479 Tabacco, L.: Airborne radio-echo sounding of the Wilkes Subglacial Basin, the Transantarctic Mountains,  
480 and the Dome C Region, *Terra Antarctica Reports*, 13, 55-63, 2007.
- 481 Corr, H., and Robinson, C.: Airborne radio-echo sounding of the English Coast, western Palmer Land, Antarctic  
482 Peninsula (2016/17 season) (Version 1.0), UK Polar Data Centre, Natural Environment Research Council,  
483 UK Research & Innovation, <https://doi.org/10.5285/E07D62BF-D58C-4187-A019-59BE998939CC>, 2020.
- 484 Daniels, D. J.: Ground penetrating radar, ( 2nd ed.). London: The Institute of Engineering and  
485 Technology, <https://doi.org/10.1049/PBRA015E>, 2004.
- 486 Dowdeswell, J. A., and Evans, S.: Investigations of the form and flow of ice sheets and glaciers using radio  
487 echo sounding, *Reports on Physics*, 67, <https://doi.org/10.1088/0034-4885/67/10/R03>, 2004.
- 488 Favier, L., Pattyn, F., Berger, S., and Drews, R.: Dynamic influence of pinning points on  
489 marine ice-sheet stability: a numerical study in Dronning Maud Land, East Antarctica, *The*  
490 *Cryosphere*, 10, 2623–2635, <https://doi.org/10.5194/tc-10-2623-2016>, 2016.
- 491 Fretwell, P., et al.: Bedmap2: Improved ice bed, surface and thickness datasets for Antarctica,  
492 *Cryosphere*, 7, 375–393, <https://doi.org/10.5194/tc-7-375-2013>, 2013.
- 493 Fürst, J. J., Durand, G., Gillet-Chaulet, F., Tavard, L., Rankl, M., Braun, M., and Gagliardini, O.: The  
494 safety band of Antarctic ice shelves, *Nature Climate Change*, 6(5), 479–482,  
495 <https://doi.org/10.1038/NCLIMATE2912>, 2016.
- 496 Gardner, A.S., Moholdt, G., Scambos, T., Fahnestock, M., Ligtenberg, S., van den Broeke, M., and Nilsson, J.:  
497 Increased West Antarctic and unchanged East Antarctic ice discharge over the last 7 years, *The Cryosphere*,  
498 12, 521–547, <https://doi.org/10.5194/tc-12-521-2018>, 2018. Gudmundsson, G. H., Krug, J., Durand, G.,  
499 Favier, L., and Gagliardini, O.: The stability of  
500 grounding lines on retrograde slopes, *Cryosphere*, 6, 1497–1505, <https://doi.org/10.5194/tc-6>  
501 -1497-2012, 2012.
- 502 Gudmundsson, G. H.: Ice-shelf buttressing and the stability of marine ice sheets, *The*  
503 *Cryosphere*, 7, 647–655, <https://doi.org/10.5194/tc-7-647-2013>, 2013.
- 504 Helm, V., Humbert, A., and Miller, H.: Elevation and elevation change of Greenland and  
505 Antarctica derived from CryoSat-2, *Cryosphere*, 8, 1539–1559, <https://doi.org/10.5194/tc-8-1539>  
506 2014, 2014.
- 507 Hogg, A. E., Shepherd, A., Cornford, S. L., Briggs, K. H., Gourmelen, N., Graham, J. A., Joughin, I.,

508 Mougnot, J., Nagler, T., Payne, A. J., Rignot, E., and Wuite, J.: Increased ice flow in  
509 Western Palmer Land linked to ocean melting, *Geophysical Research Letters*, 44, 4159-4167,  
510 <https://doi.org/10.1002/2016GL072110>, 2017.

511 Jamieson, S. S. R., Vieli, A., Livingstone, S. J., Cofaigh, C. O., Stokes, C., Hillenbrand, C.-D., and  
512 Dowdeswell, J. A.: Ice-stream stability on a reverse bed slope, *Nature Geoscience*, 5, 799  
513 802, <https://doi.org/doi:10.1038/ngeo1600>, 2012.

514 Kimura, S., Nicholls, K. W., and Venables, E.: Estimation of ice shelf melt rate in the presence of a  
515 thermohaline staircase, *Journal of Oceanography*, 45, 133–148, <https://doi.org/10.1175/JPO-D-13-0219.1>,  
516 (2015).

517 Kleman, J., and Applegate, P. J.: Durations and propagation patterns of ice sheet instability  
518 events, *Quaternary Science Reviews*, 92, 32-39, <https://doi.org/10.1016/j.quascirev.2013.07.030>,  
519 2014.

520 Konrad, H., Shepherd, A., Gilbert, L., Hogg, A. E., McMillan, M., Muir, A., and Slater, T.:  
521 Net retreat of Antarctic glacier grounding lines. *Nature Geoscience*, 11, 258–262,  
522 <https://doi.org/10.1038/s41561-018-0082-z>, 2018.

523 Kowal, K. N., Pegler S. S., and Worster, M. G.; Dynamics of laterally confined marine ice  
524 sheets. *Journal of Fluid. Mechanics*, 790(R2), 1–14, <https://doi.org/10.1017/jfm.2016.37>, 2016.

525 Lythe, M. B., Vaughan, D. G., and the BEDMAP Consortium; A new ice thickness and  
526 subglacial topographic model of Antarctica. *Journal of Geophysical Research: Solid Earth*, 106  
527 (B6), 11,335-11,351, <https://doi.org/10.1029/2000JB900449>, 2001.

528 MacGregor, J. A., Anandakrishnan, S., Catania, G. A., Winebrenner, D. P.; The grounding  
529 zone of the Ross Ice Shelf, West Antarctica, from ice-penetrating radar. *Journal of Glaciology*, 57  
530 (205), 917-928, <https://doi.org/10.3189/002214311798043780>, 2011.

531 Martín-Español, A., Zammit-Mangion, A., Clarke, P. J., Flament, T., Helm, V., King, M. A., Luthcke,  
532 S. B., Petrie, E., Rémy, F., Schön, N., Wouters, B., and Bamber, J. L.: Spatial and temporal  
533 Antarctic Ice Sheet mass trends, glacio-isostatic adjustment, and surface processes from a joint  
534 inversion of satellite altimeter, gravity, and GPS data, *Journal of Geophysical Research: Earth  
535 Surface*, 121, 182–200, <https://doi.org/10.1002/2015JF003550>, 2016.

536 McMillan, M., Shepherd, A. Sundal, A., Briggs, K., Muir, A. Ridout, A. Hogg, A., and Wingham, D.:  
537 Increased ice losses from Antarctica detected by CryoSat-2, *Geophysical Research Letters*,  
538 41, 3899–3905, <https://doi.org/10.1002/2014GL060111>, 2014.

539 Minchew, B. M., Gudmundsson, G. H., Gardner, A. S., Paolo, F. S., and Fricker, H. A.:  
540 Modeling the dynamic response of outlet glaciers to observed ice shelf thinning in the  
541 Bellingshausen Sea Sector, West Antarctica, *Journal of Glaciology*, 64(244), 333-342,  
542 <https://doi.org/10.1017/jog.2018.24>, 2018.

543 Morlighem, M.: MEaSURES BedMachine Antarctica, Version 1. Boulder, Colorado USA.  
544 NASA National Snow and Ice Data Center Distributed Active Archive Center,  
545 <https://doi.org/10.5067/C2GFER6PTOS4>, 2019.

546 Morlighem, M., et al.: Deep glacial troughs and stabilizing ridges unveiled beneath the  
547 margins of the Antarctic ice sheet, *Nature Geoscience*, 13, 132-137,

548 <https://doi.org/10.1038/s41561-019-0510-8>, 2019.

549 Mougnot, J., Rignot, E., and Scheuchl, B.: Continent-wide, interferometric SAR phase,  
550 mapping of Antarctic ice velocity, *Geophysical Research Letters*, 46, 9710–9718,  
551 <https://doi.org/10.1029/2019GL083826>, 2019.

552 Paden, J., Li, J., Leuschen, C., Rodriguez-Morales, F., and Hale, R.: IceBridge MCoRDS L2 Ice Thickness,  
553 Version 1. [English Coast of Western Palmer Land, Antarctica], Boulder, Colorado USA, NASA National  
554 Snow and Ice Data Center. Distributed Active Archive Center, <https://doi.org/10.5067/GDQ0CUCVTE2Q>  
555 2010, updated 2019.

556 Pritchard, H. D., Ligtenberg, S. R. M., Fricker, H. A., Vaughan, D. G., van den Broeke, M. R., and  
557 Padman, L.: Antarctic ice-sheet loss driven by basal melting of ice shelves, *Nature*, 484,  
558 502–505, <https://doi.org/10.1038/nature10968>, 2012.

559 Rignot, E.: Changes in West Antarctic ice stream dynamics observed with ALOS PALSAR data, *Geophysical*  
560 *Research Letters*, 35, L12505, <https://doi.org/10.1029/2008GL033365>, 2008.

561 Rignot, E., Mougnot, J., Scheuchl, B., van den Broeke, M., van Wessem, M. J., and Morlighem, M.:  
562 Four decades of Antarctic Ice Sheet mass balance from 1979–2017, *Proceedings of the*  
563 *National Academy of Sciences*, 116(4), 1095–1103, <https://doi.org/10.1073/pnas.1812883116>,  
564 2019.

565 Rosier, S. H. R., and Gudmundsson, G. H.: Tidal bending of ice shelves as a mechanism for  
566 large-scale temporal variations in ice flow, *The Cryosphere*, 12(5), 1699–1713,  
567 <https://doi.org/10.5194/tc-12-1699-2018>, 2018.

568 Schoof, C.: Ice sheet grounding line dynamics: steady states, stability and hysteresis, *Journal*  
569 *of Geophysical Research*, 112, F03S28, <https://doi.org/10.1029/2006JF000664>, 2007.

570 Shepherd, A., Wingham, D., Mansley, J. A., D.: Inland thinning of the Amundsen Sea sector, West Antarctica,  
571 *Geophysical Research Letters*, 29(10), 1364, <https://doi.org/10.1029/2001GL014183>, 2002.

572 Smith, B., and 14 others.: Pervasive ice sheet mass loss reflects competing ocean and  
573 atmosphere processes, *Science*, <https://doi.org/10.1126/science.aaz5845>, 2020.

574 Tsai, V. C., Stewart, A. L., and Thompson, A. F.: Marine ice-sheet profiles and stability under  
575 coulomb basal conditions, *Journal of Glaciology*, 61 (226), 205–215,  
576 <https://doi.org/10.3189/2015JoG14J221>, 2015.

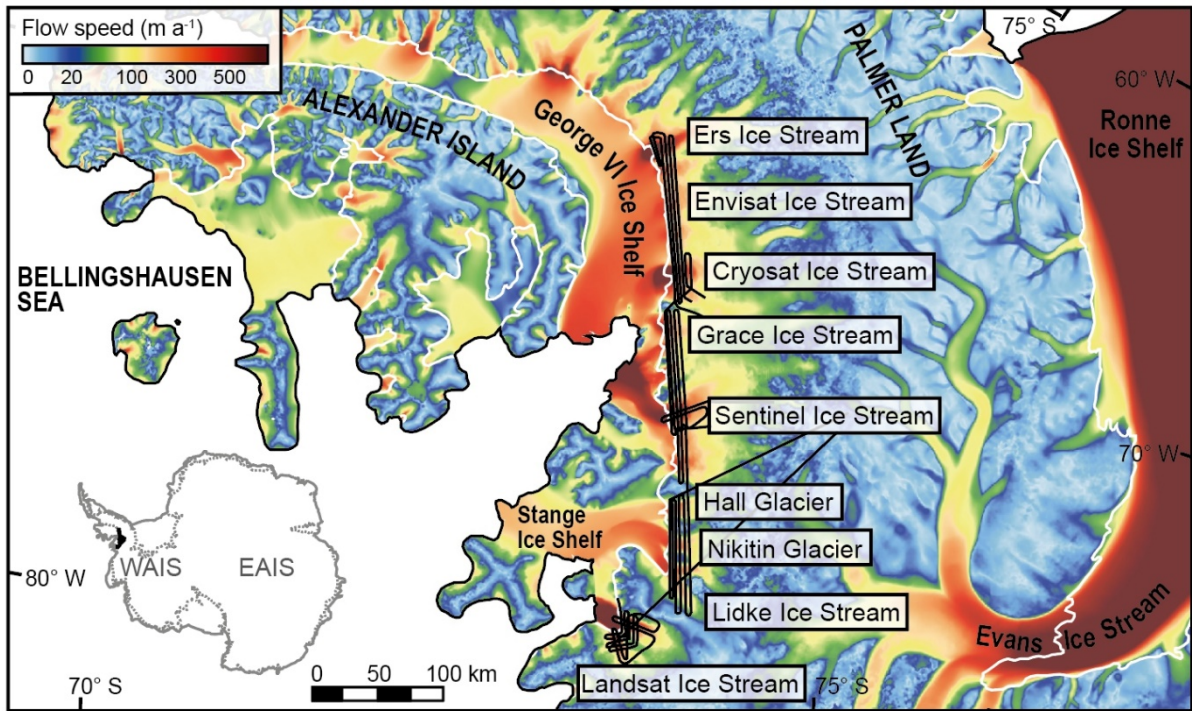
577 van Wessem, J. M., and 13 others: Improved representation of East Antarctic surface mass  
578 balance in a regional atmospheric climate model, *Journal of Glaciology*, 60 (222), 761–770,  
579 <https://doi.org/10.3189/2014JoG14J051>, 2014.

580 van Wessem, J. M., Ligtenberg, S. R. M., Reijmer, C. H., van de Berg, W. J. van den Broeke, M. R.,  
581 Barrand, N. E., Thomas, E. R., Turner, J., Wuite, J., Scambos, T. A., and van Meijgaard, E.:  
582 The modelled surface mass balance of the Antarctic Peninsula at 5.5 km horizontal resolution,  
583 *Cryosphere*, 10(1), 271–285, <https://doi.org/10.5194/tc-10-271-2016>, 2016.

584 Vaughan, D. G., Corr, H. F. J., Ferraccioli, F., Frearson, N., O’Hare, A., Mach, D., Holt, J. W., Blankenship, D.  
585 D., Morse, D. L., and Young, D. A.: New boundary conditions for the West Antarctic ice sheet: Subglacial  
586 topography beneath Pine Island Glacier, *Geophysical Research Letters*, 330, 2–5,  
587 <https://doi.org/10.1029/2005GL025588>, 2006.

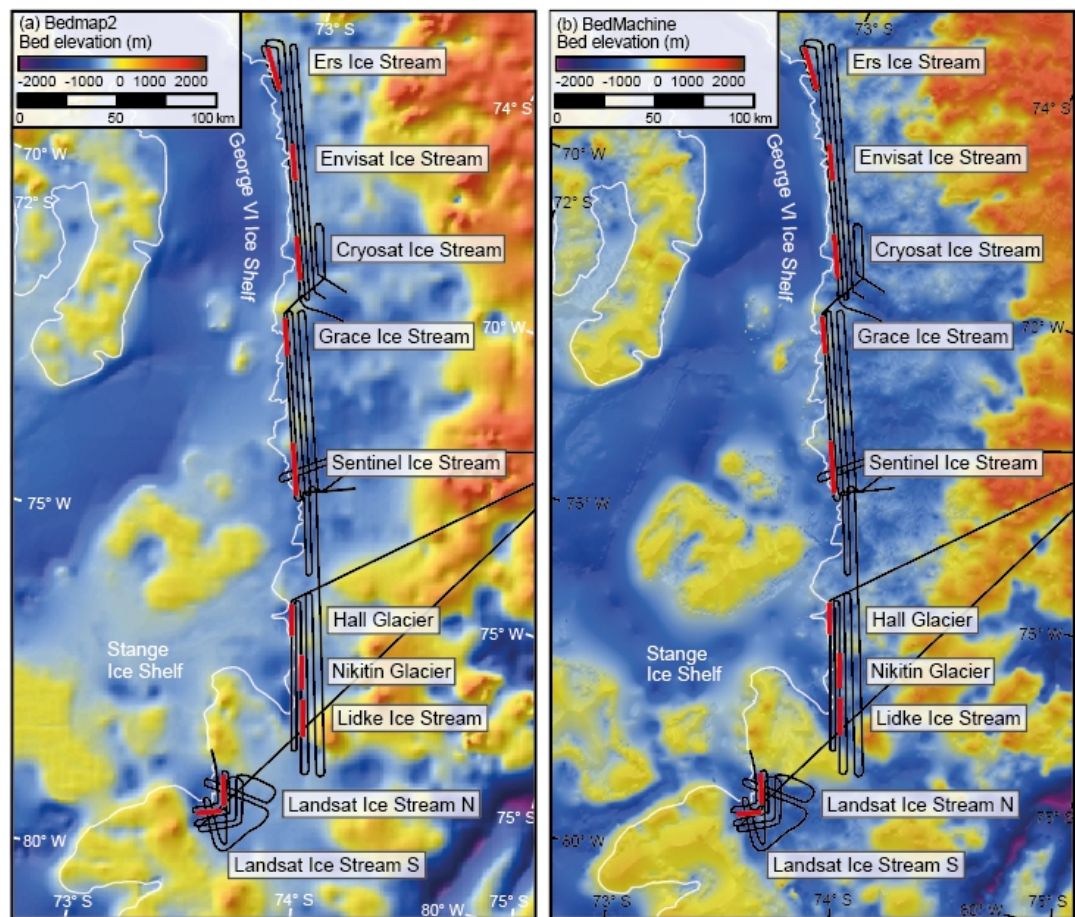
- 588 Weertman, J.: Stability of the junction of an ice sheet and ice shelf, *Journal of Glaciology*, 13  
589 (67), 3-11, <https://doi.org/10.3189/S0022143000023327>, 1974.
- 590 Wouters, B., Martín-Español, A., Helm, V., Flament, T., van Wessem, J. M., Ligtenberg, S. R. M.,  
591 van den Broeke, M. R., and Bamber, J. L.: Dynamic thinning of glaciers on the Southern  
592 Antarctic Peninsula, *Science*, 348, 899–903, <https://doi.org/10.1126/science.aaa5727>, 2015.





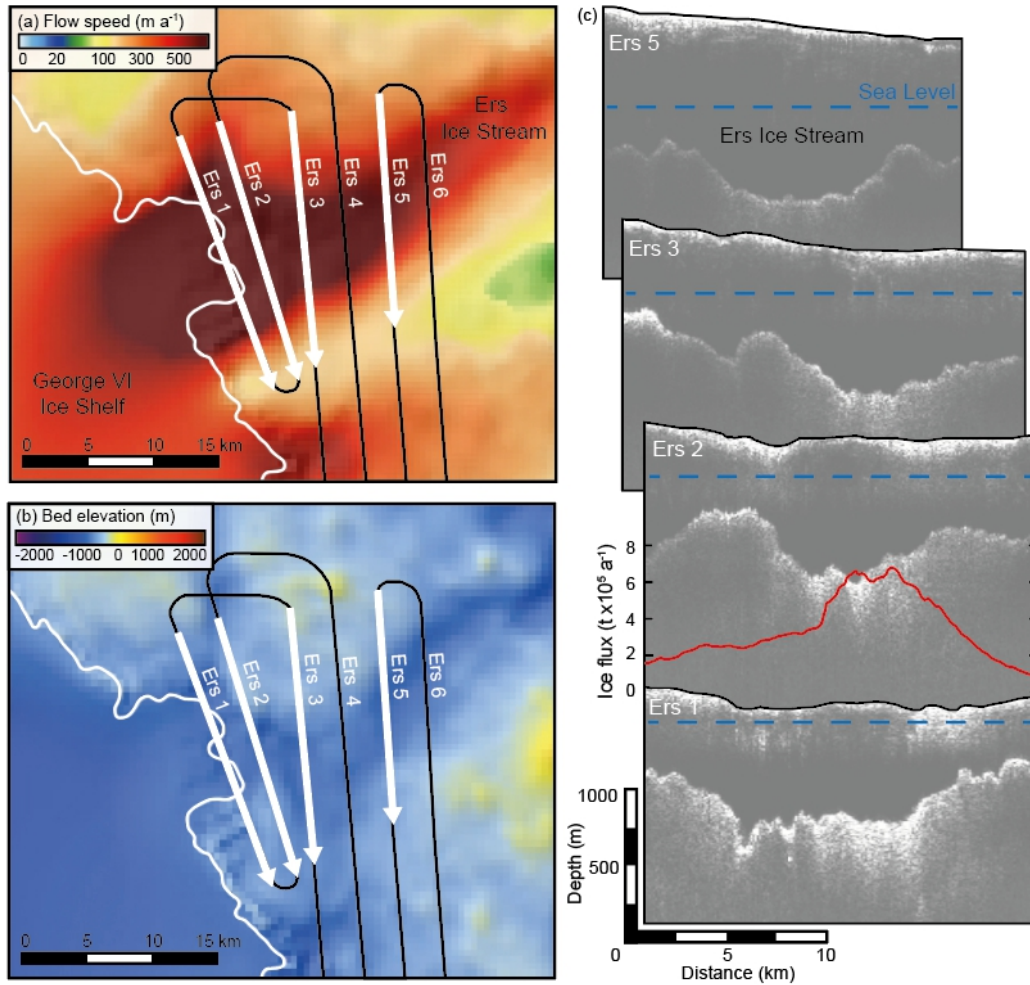
593  
594

595 **Figure 1.** Airborne radio-echo sounding surveys (RES) (black lines), collected during the austral summer of  
 596 2016/2017, transcend the Bellingshausen Sea sector of Palmer Land in the Antarctic Peninsula. RES surveys  
 597 transect several glaciers and ice streams along the English Coast at, or close to the Antarctic Surface Accumulation  
 598 and Ice Discharge (ASAID) grounding line (white line) (Bindschadler et al., 2011), after which the ice floats.  
 599 Background imagery shows surface flow speeds from MEaSURES (Mouginot et al., 2019). The inset map shows  
 600 the location of RES surveys used in this paper (black), superimposed on a map of Antarctica.



601  
 602  
 603  
 604  
 605  
 606  
 607  
 608  
 609  
 610

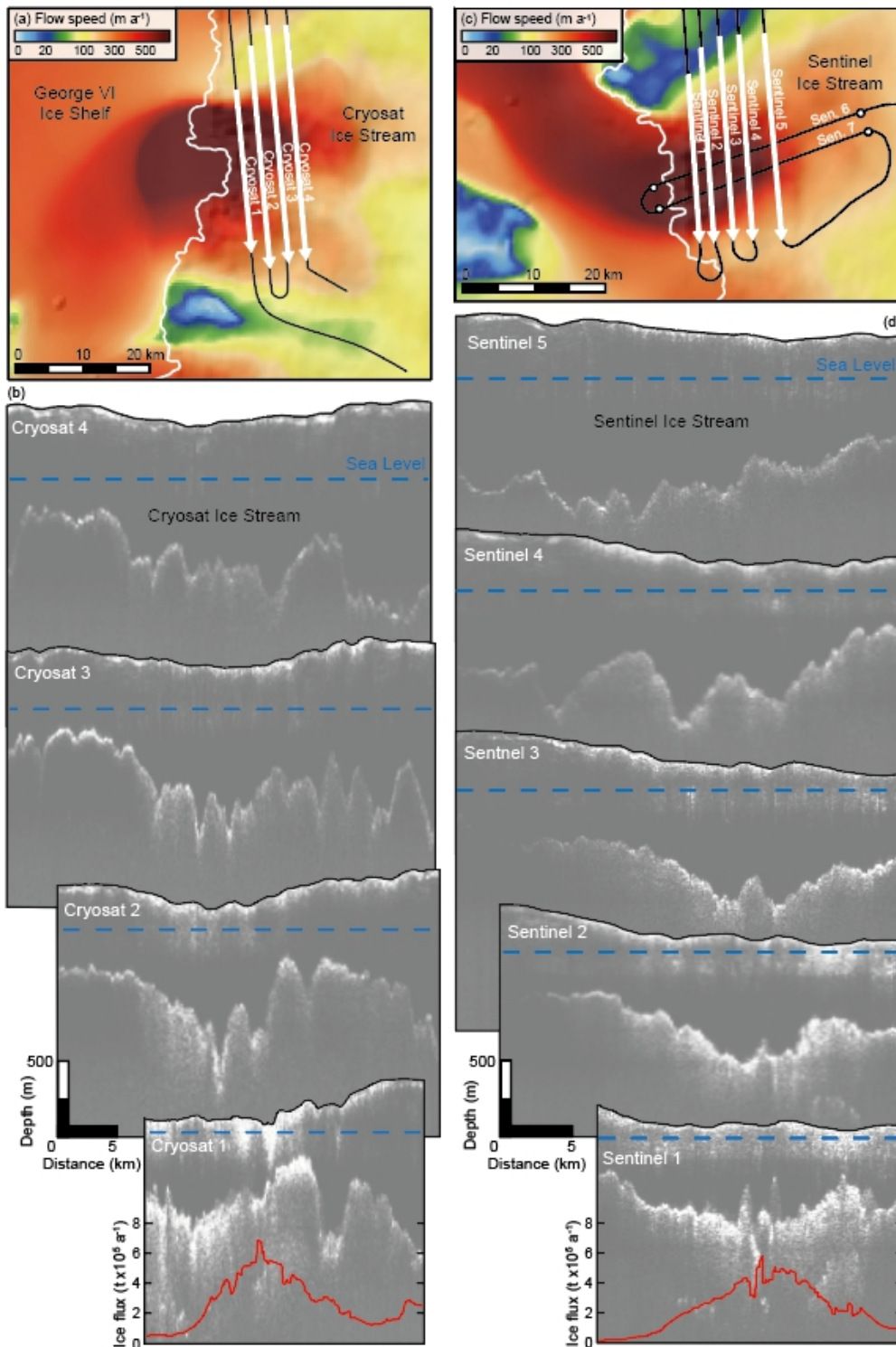
**Figure 2.** Major outlet glacier and ice stream flux gates (red) along the English Coast of Palmer Land. Subglacial topography maps from Bedmap2 (Fretwell et al., 2013) and BedMachine (Morlighem, 2019) are presented in panels (a) and (b). Black lines denote airborne RES transects detailed in this paper, whilst the white line shows the location of the ASAID grounding line (Bindschadler et al., 2011). Both maps show that subglacial topography frequently rests well below sea level along the English Coast. Panel (c) compares ice flux measurements (in gigatons), derived from Bedmap2 ice thickness data (Fretwell et al., 2013) (light-grey bars), our direct radar measurements (dark-grey bars) and ice thickness data from BedMachine (Morlighem, 2019) (mid-grey bars). These calculations utilise the same flux gates, noted in (a) and (b).



611

612

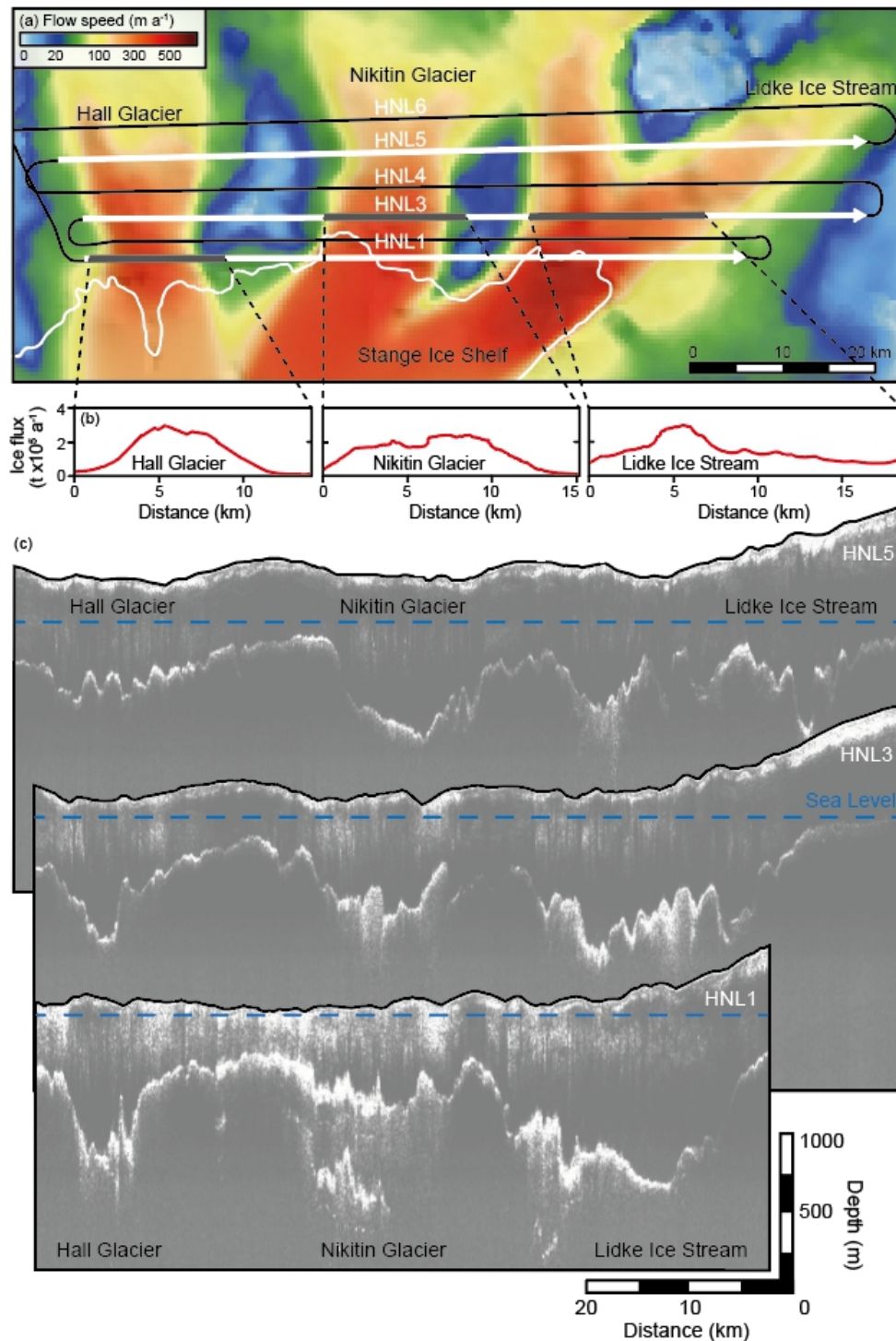
613 **Figure 3.** Ice penetrating radar transects (black lines) across Ers Glacier, superimposed on a map of surface flow  
 614 speeds (Mouginot et al., 2019) (a) and subglacial topography from BedMachine (Morlighem, 2019) (b). White  
 615 arrows indicate the location and direction of radargrams presented in (c) whilst the white line indicates the ASAID  
 616 grounding line (Bindschadler et al., 2011). Ice flux across RES transect Ers 2 is displayed as a red line in (c). Note  
 617 that the scale is in tonnes  $\times 10^5$ . c) Radargrams reveal surface topography, ice thickness and the subglacial bed  
 618 (recorded as diffuse white reflectors). Sea level is marked by a blue dashed line.



619

620

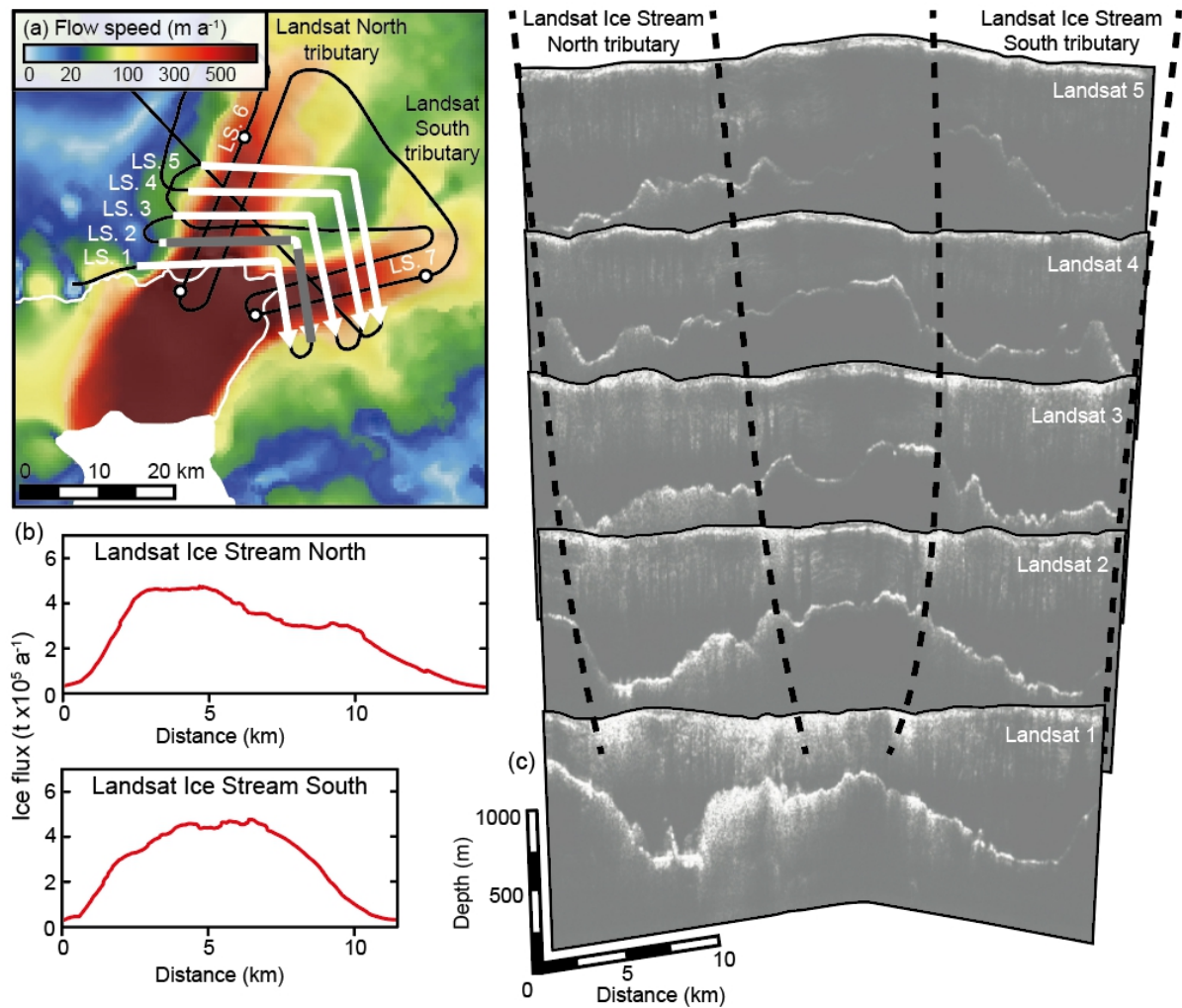
621 **Figure 4.** Radar investigations of Cryosat and Sentinel ice streams. Surface flow speed maps (Mouginot et al.,  
 622 2019) reveal the spatial variability in flow in panels (a) and (c). These panels highlight the location of radargrams  
 623 collected along the English Coast (black lines) as well as the direction and location of radargrams (white arrows)  
 624 displayed in (b) and (d). White lines indicate the ASAID grounding line (Bindschadler et al., 2011) whilst white  
 625 circles in (c) represent the extent of along-flow radar transects presented in Figure 7. Red lines in (b) and (d) show  
 626 calculated ice flux along RES transects Cryosat 1 and Sentinel 1. Sea level is marked by a blue dashed line.



627

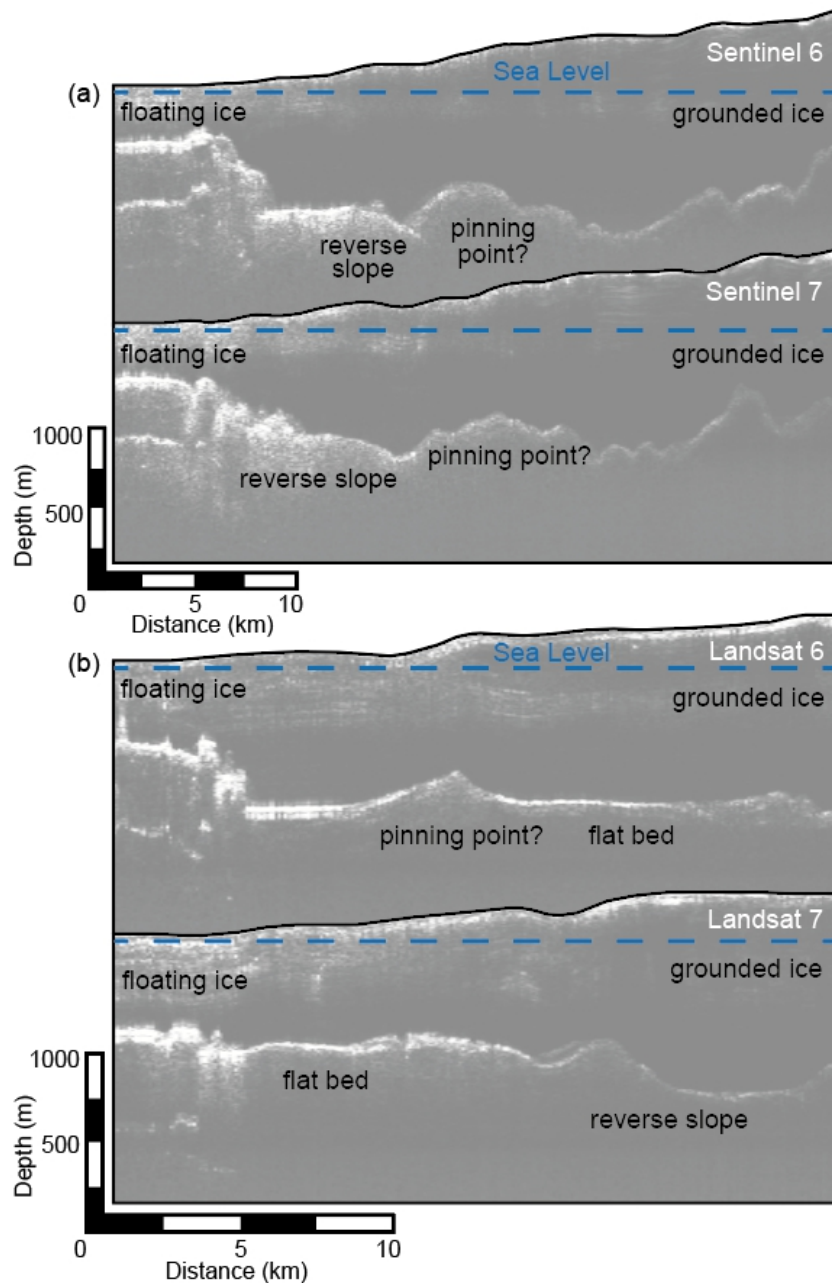
628

629 **Figure 5.** Hall Glacier, Nikitin Glacier and Lidke Ice Stream transfer fast flowing ice to the local grounding line  
 630 (white), where ice flow coalesces in the Stange Ice Shelf. (a) surface flow speeds from Mouginot et al. (2019),  
 631 superimposed with English Coast radargram tracks (black), white arrows to indicate the location and direction of  
 632 radargrams presented in (c), and thick grey lines to note ice flux gates, graphed in (b). The white line indicates the  
 633 ASAID grounding line (Bindschadler et al., 2011). Note that the map has been rotated 90 degrees from its true  
 634 orientation (shown in Figure 1). Radargrams in (c) reveal changes in ice thickness and subglacial topography  
 635 down flow. Sea level is marked by a blue dashed line.



636  
637

638 **Figure 6.** Landsat Ice Stream is fed by northern and southern tributaries which coalesce at the grounding zone.  
 639 These discrete flow units are clearly visible in (a) which shows a map of surface flow speeds from Mouginot et  
 640 al. (2019). Black lines show the density of RES transects in this location, whilst white arrows show the location  
 641 and orientation of transects displayed in (c). In panel (a) the white line represents the ASAID grounding line  
 642 (Bindschadler et al., 2011) whilst thick grey lines show the location of flux gates, presented in (b). White circles  
 643 on panel (a) represent the extent of along-flow radar transects presented in Figure 7 (where sea level is marked  
 644 along each tributary). Radargrams in (c) show how the two ice stream tributaries (approximately marked by a  
 645 black dashed line) are separated by relatively high elevation subglacial topography.



646

647

648 **Figure 7.** Along-flow radar transects of Sentinel Ice Stream (a) and Landsat Ice Stream (b). Transect locations  
 649 are marked by circles in Figures 4c and 6a. All four radargrams reveal a general pattern of surface lowering and  
 650 ice sheet thinning down flow (from right to left). Bright, white, diffuse reflectors on the left-hand side of the  
 651 radargrams represent floating ice and water ingress. Annotations highlight these features, and basal conditions.  
 652 Sea level is marked by a blue dashed line.